









RESEARCH ARTICLE OPEN ACCESS

In Situ Photocorrosion Assessment of Protected Hematite Photoanodes During Accelerated Stress Tests

Victoria Benavente Llorente¹  | Ken J. Jenewein^{1,2}  | André Hofer³  | Andreas Körner^{1,2}  | Andreas Hutzler¹  | Attila Kormányos⁴  | Julien Bachmann³  | Serhiy Cherevko¹ 

¹Helmholtz-Institute Erlangen-Nürnberg for Renewable Energy (IET-2), Forschungszentrum Jülich GmbH, Erlangen, Germany | ²Department of Chemical and Biological Engineering, Friedrich-Alexander-Universität Erlangen-Nürnberg (FAU), Erlangen, Germany | ³Department of Chemistry and Pharmacy, Materials Chemistry section, Chair Chemistry of Thin Film Materials, IZNF, Friedrich-Alexander-Universität Erlangen-Nürnberg, Erlangen, Germany | ⁴Department of Physical Chemistry and Materials Science, Interdisciplinary Excellence Centre, University of Szeged, Szeged, Hungary

Correspondence: Victoria Benavente Llorente (victoria.benavente@unc.edu.ar) | Attila Kormányos (kormanyos.attila@szte.hu) | Serhiy Cherevko (s.cherevko@fz-juelich.de)

Received: 20 August 2025 | **Revised:** 2 October 2025 | **Accepted:** 15 October 2025

Keywords: atomic layer deposition | hematite | online-ICP-MS | photoelectrochemistry | scanning flow cell

ABSTRACT

Nanostructured α -hematite (Fe_2O_3) is a widely studied material for photoanode applications, particularly for driving the oxygen evolution reaction (OER) under visible light irradiation in photoelectrochemical (PEC) cells. Our recent work has shown that Fe_2O_3 suffers from photocorrosion in alkaline and neutral electrolytes, with a noticeable decline in performance after 5 h of operation. This highlights the need for strategies that enhance the stability of Fe_2O_3 -based photoanodes. To enhance the stability of Fe_2O_3 nanorods (NR), we employed atomic layer deposition (ALD) to coat the NR with a well-defined, controlled TiO_2 overlayer designed to protect the photoanode from photocorrosion during PEC operation. The influence of overlayer thickness is evaluated regarding the PEC activity, stability, and photocurrent retention in alkaline electrolyte using a PEC scanning flow cell coupled to an inductively coupled plasma mass spectrometer (PEC-ICP-MS). This setup can quantify metal dissolution during PEC OER, allowing the characterization of the photo-degradation under realistic illumination conditions. An accelerated stress test (AST) protocol was designed to drive degradation faster and obtain insightful information about the stability of the $\text{TiO}_2/\text{Fe}_2\text{O}_3$ heterostructures using in situ PEC-ICP-MS. PEC-ICP-MS measurements demonstrate that the TiO_2 coating significantly enhances the photocorrosion resistance of Fe_2O_3 NR in alkaline electrolytes during operation. A TiO_2 thickness of 2.8 nm (50 ALD cycles) offered the most favorable compromise between activity, photocurrent retention, and decrease of Fe dissolution. The proposed methodology combines in situ stability quantification and ASTs as a powerful tool to advance material development and can be extended to other protected photoanodes.

1 | Introduction

Sunlight is a promising renewable energy source essential for transitioning to sustainable energy solutions. However, the intermittent nature of solar energy presents a significant challenge, requiring efficient energy storage technologies. One promising approach to tackle this shortcoming is the production of solar fuels through photoelectrochemical (PEC) devices. PEC cells allow the storage

of solar energy directly into small molecules such as “green hydrogen” or methanol, which are prominent sustainable fuels [1, 2].

Hematite nanorods (Fe_2O_3 NR) have garnered significant attention as a photoanode material due to the high natural abundance of iron, strong absorption in the visible spectrum, and the versatility of their properties, which can be easily tuned using a simple, low-cost hydrothermal synthesis method [3–5].

This is an open access article under the terms of the [Creative Commons Attribution](https://creativecommons.org/licenses/by/4.0/) License, which permits use, distribution and reproduction in any medium, provided the original work is properly cited.

© 2025 The Author(s). *Solar RRL* published by Wiley-VCH GmbH.

The stability of photoanode materials is a serious barrier that hinders the commercial viability of PEC cells [6–8]. The lifetime of the employed metal oxide photoanodes used as photoabsorbers, such as Fe_2O_3 , WO_3 , and BiVO_4 , is limited by photocorrosion. The active dissolution of metals during the PEC oxygen evolution reaction (OER) was unveiled using an operando technique, a PEC scanning flow cell coupled to an inductively coupled plasma mass spectrometer (PEC-ICP-MS) [9–15]. To make photoelectrochemical processes competitive, it is essential to decrease the metal leaching of the photoabsorbers during operation.

Various strategies have been investigated to enhance the stability of photoanode materials. Among these, modifying the electrolyte composition has shown a significant influence on photoanode stability, as demonstrated for materials such as BiVO_4 and WO_3 . In the case of WO_3 , the presence of different reactive intermediates in different electrolytes has been identified as a key factor affecting its stability [11]. For BiVO_4 , variations in dissolution rates were found to correlate with changes in surface chemistry and morphology, both of which are strongly influenced by the electrolyte [16].

In our recent study, we evaluated the stability of Fe_2O_3 NR in buffered and unbuffered electrolytes at neutral and alkaline pHs [15]. Using PEC-ICP-MS, we observed notable Fe dissolution in unbuffered electrolytes under both neutral and alkaline pH conditions. The highest dissolution rate was obtained in 50 mM NaOH, which is widely used as a standard electrolyte for characterizing the PEC performance of Fe_2O_3 NR. While buffered electrolytes containing phosphate salts appeared to suppress Fe dissolution in the short term, long-term experiments at neutral pH revealed photoanode degradation and P incorporation to the surface.

These findings suggest that improving the stability of Fe_2O_3 NR requires strategies beyond merely altering the electrolyte composition. One approach involves the fabrication of heterostructures by coating the Fe_2O_3 NR with thin layers (0.5–5 nm) of wide bandgap semiconductors, such as TiO_2 (3.2 eV) [6, 17–21]. The thin TiO_2 coating prevents contact between the photoabsorber and the electrolyte, alleviating photocorrosion. It is already described in the literature that the coating of Fe_2O_3 nanostructures with TiO_2 improves the chemical stability when exposed to strongly acidic media [18, 19]. However, information on the improvement of the stability of $\text{Fe}_2\text{O}_3/\text{TiO}_2$ heterostructures using in situ PEC techniques should be advanced, as only a few reports have evaluated the stability of Fe_2O_3 nanostructures using ex situ quantification of Fe dissolution [17, 18, 22, 23]. Moreover, most stability studies on $\text{Fe}_2\text{O}_3/\text{TiO}_2$ heterostructures have not addressed alkaline electrolytes, and our previous work revealed the highest dissolution rates for the Fe_2O_3 NR during PEC operation [15]. Therefore, it is of utmost importance to gather information of the stability and dissolution kinetics of both constituents (i.e., Fe_2O_3 and the TiO_2 overlayers) in such electrolytes under operating conditions.

This study aims to enhance the stability of Fe_2O_3 NR by depositing thin TiO_2 coatings and to investigate the relationship between stability and activity in an alkaline electrolyte as a function of TiO_2 thickness, using in situ PEC-ICP-MS. The deposition of the TiO_2 layer was performed using atomic layer deposition (ALD), as this technique ensures precise control over film

thickness at the Ångström scale by changing the cycle number, offering a promising pathway to enhance the stability of PEC systems without compromising their efficiency [18, 20, 24, 25].

In photoelectrochemical research, degradation tests are typically conducted through long-duration experiments under constant illumination and a constant potential (or current density) [3, 5, 26, 27]. While widely used, this approach is time-consuming and unsuited for advanced degradation analyses employing in situ techniques. As an alternative, accelerated stress tests (ASTs) speed up the degradation process by applying controlled stress protocols within the operational range intended for the material under study [28–32]. Besides, ASTs can be designed to be combined with in situ ICP-MS [33, 34]. Therefore, in this work, we propose using ASTs as a versatile tool suitable for PEC-ICP-MS online measurements.

We observed a decrease in the activity of the $\text{Fe}_2\text{O}_3/\text{TiO}_2$ as the TiO_2 thickness increased. Also, an annealing step after ALD is crucial for enhancing the performance of the heterostructures, particularly for thicker TiO_2 layers. PEC-ICP-MS successfully identified the decrease in Fe dissolution upon Fe_2O_3 NR protection. Stability measurements using PEC-ICP-MS revealed differing trends between a single cyclic voltammetry (CV) scan and the AST, offering valuable insights into the impact of startup and shutdown cycles simulated with potential pulses. Using this approach, we found a tradeoff between activity, stability, and photocurrent retention, observing that a layer of 2.8 ± 0.5 nm (50 ALD cycles) of TiO_2 appears to be the optimal choice to protect the Fe_2O_3 NR for PEC applications.

2 | Results and Discussion

2.1 | Preparation and Structural Characterization of $\text{Fe}_2\text{O}_3/\text{TiO}_2$ Core-Shell Photoelectrocatalysts

Herein, Fe_2O_3 nanorods were prepared employing an optimized hydrothermal method introduced in our previous work [15]. The photoanode consists of homogeneously distributed Fe_2O_3 NR supported on FTO. The high-angle annular dark field scanning transmission electron microscopy (HAADF-STEM) image presented in Figure 1a shows hematite nanorods with a length of 170 ± 30 nm and a width of 100 ± 10 nm, similar to the nanorods characterized in the mentioned study. STEM energy-dispersive X-ray spectrum (EDXS) imaging reveals the Fe signal of the hematite particles and some Sn residues that were probably introduced from the substrate (possibly scratched out during sample preparation).

To study the influence of the thickness on activity and stability of the $\text{Fe}_2\text{O}_3/\text{TiO}_2$ heterostructures, different numbers of ALD cycles (25, 50, and 75) were used to coat the Fe_2O_3 NR with a thin layer of TiO_2 . Figure 1a displays HAADF-STEM images and corresponding STEM EDX spectrum images of the $\text{Fe}_2\text{O}_3/\text{TiO}_2$ with 25 cycles, where the TiO_2 layer is rough and barely visible and perhaps not fully closed. However, the TiO_2 layer can be clearly identified for 50 or 75 ALD cycles, with the titania layer showing a different Z contrast due to the different atomic masses of Fe and Ti. The corresponding STEM-EDX

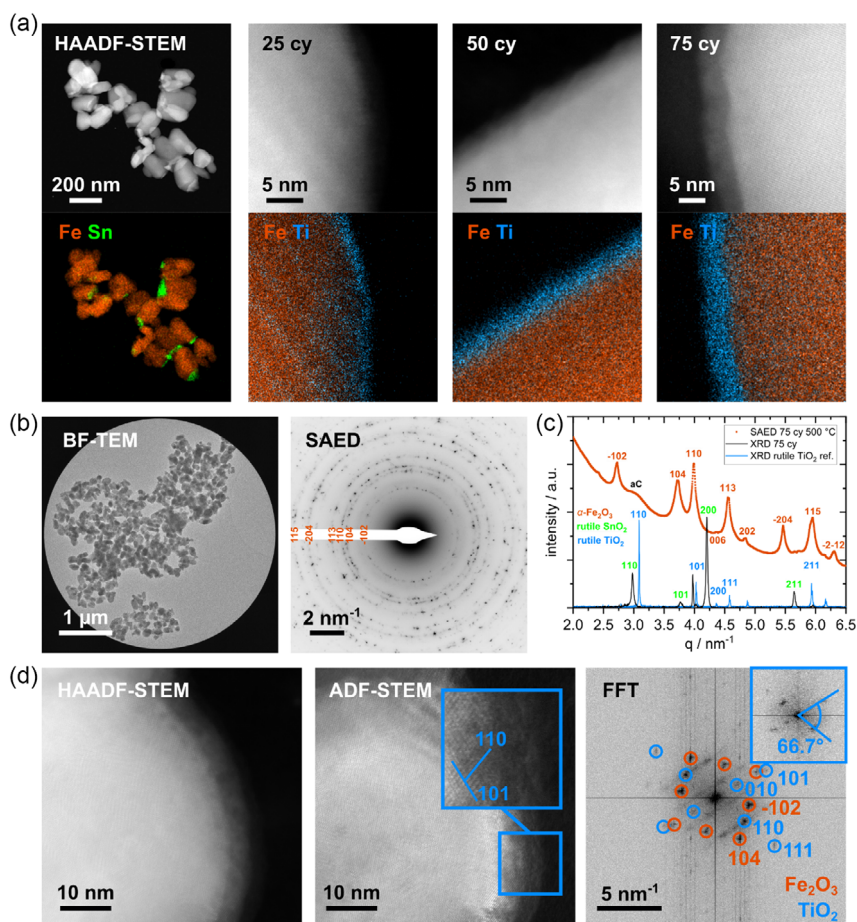


FIGURE 1 | (a) HAADF-STEM and corresponding STEM-EDX spectrum images of bare Fe₂O₃ nanorods (Fe and Sn signal) and Fe₂O₃ nanorods coated with 25, 50, and 75 ALD cycles of TiO₂ (Fe and Ti signal). (b) Bright field TEM image and corresponding selected area electron diffraction pattern of titania-coated hematite particles. (c) Integrated SAED and XRD spectrum with an additional reference XRD spectrum of rutile TiO₂ [43], and (d) high-resolution HAADF-STEM and ADF-STEM image with corresponding diffractogram. The inset with the blue frames depicts which spots belong to the titania phase and the hematite phase, respectively.

spectrum images in Figure 1a confirm the presence of a homogenous TiO₂ coating encapsulating the nanorod structure for all ALD cycles. Therefore, the preparation conditions used yielded a core-shell type of heterostructure presenting a conformal and continuous distribution of a TiO₂ layer for all samples.

It is well defined in literature that a postannealing treatment can promote the diffusion of Ti(IV) ions into the Fe₂O₃ crystal structure, leading to a doping effect that can improve the PEC performance of the photoanodes [35–37]. To exclude this scenario, STEM-EDX spectra were recorded. Results are presented in Figure S1 along with the corresponding Ti and Fe line profiles of individual particles of the heterostructures prepared with 75 cycles for a sample as prepared and a sample annealed after ALD. Following annealing, the TiO₂ layer remains conformal (i.e., the Ti signal remains flat despite the increasing Fe signal toward the particle's center), indicating that the core-shell structure is preserved after exposure to 500°C for 30 min. This observation aligns with literature reports, which suggest that significant solid-state reaction of TiO₂ and Fe₂O₃ typically occurs only at annealing temperatures exceeding 500°C.

The thickness of the TiO₂ coating was determined from STEM images, each sample presenting different ALD cycles, and the results are presented in Figure S2. The average thickness increases from 1.5 ± 0.2 nm for 25 cycles, over 2.8 ± 0.5 nm for 50 cycles, to 4.7 ± 0.6 nm for 75 cycles, indicating a continuous growth with the number of ALD cycles. In addition, spectroscopic ellipsometry yields very similar results of film thicknesses deposited on monitor wafers of 1.7 and 2.6 nm for 25 and 50 ALD cycles (considering the 0.6 nm per cycle growth rate, 4.5 nm is expected for 75 cycles). The larger uncertainties originate from films not being fully closed (visible from the rough surface), different growth rates on individual crystal planes, and a convolution of the real structure with the electron probe. The electron probe has a finite size of roughly 1.2 nm (full-width at tenth maximum) [38] and is, thus, of a very similar size to the TiO₂ layer, slightly broadening the measured thickness while the error margin still overlaps with the result of the ellipsometry measurement.

To characterize the crystal structure of the photoelectrocatalyst heterostructure, XRD was performed on the Fe₂O₃@TiO₂ photoanodes. As a representative sample, the diffractogram of the samples coated with 75 cycles is shown in Figure S3. The reflections

found in the XRD pattern mainly indicate the presence of SnO_2 related to the substrate. The prominent (110) diffraction peak associated with hematite indicates that the Fe_2O_3 NR are aligned along [110] direction on the substrate, perpendicular to the FTO surface [39, 40], which was also revealed by the cross-section images presented in our previous work [15]. No signals related to the crystalline phase of TiO_2 were detected using XRD, since the crystallites are too small compared to those of hematite and SnO_2 . Additional STEM-EDXS analysis of the whole $\text{Fe}_2\text{O}_3/\text{TiO}_2 - \text{SnO}_2$ layer stack on silicon substrate is shown in Figure S4 in the Supporting Information.

To delve deeper into the crystalline structure characterization, selected area electron diffraction (SAED) on a smaller scale was recorded from an area shown in Figure 1b, and SAED results are plotted alongside the XRD spectrum in Figure 1c. The distortion-corrected SAED pattern [41] of the catalyst particles, in turn, confirms the presence of a hematite phase ($\alpha\text{-Fe}_2\text{O}_3$); however, it does not allow for an identification of the titania phase. The crystallites in the coating are very small and their total volume fraction only amounts to roughly 2% (see discussion in S4), leading to small diffraction amplitudes (intensity scales roughly with the crystallite volume) [42]. To reveal the crystal phase of the titania coating, we performed lattice imaging using high resolution HAADF-STEM and annular dark field STEM (ADF-STEM), with the results shown in Figure 1d. Diffractograms of the whole structure and the coating only (blue box) revealed that some lattice planes of TiO_2 were resolved.

Comparison with known crystal phases enabled us to identify the titanium oxide phase, which appears to be rutile TiO_2 . Four d-spacings were indexed as (101) (measured: 2.46 Å, theory: 2.50 Å), (110) (measured: 3.36 Å, theory: 3.29 Å), (111) (measured: 2.21 Å, theory: 2.20 Å), and (010) (measured: 4.71 Å, theory: 4.65 Å) planes [43]. The angle between (101) and (110) planes was determined to 66.7° (theory: 67.64°). By looking at the position of the identified peaks in reciprocal space (Figure 1c, blue line representing a reference XRD pattern of rutile TiO_2) [43], it gets evident, why an identification from the recorded SAED patterns is challenging: three of the four peaks are superimposed by very intense peaks of the hematite and the fourth one lies within the amorphous carbon signal originating from the TEM grid.

It can be concluded that the conditions and number of ALD cycles used in this work yield samples with distinct and well-characterized TiO_2 thicknesses to study the impact of different overlayers on the activity and stability of $\text{TiO}_2/\text{Fe}_2\text{O}_3$ heterostructures.

2.2 | Photoelectrochemical Characterization of $\text{Fe}_2\text{O}_3/\text{TiO}_2$ Using the Scanning Flow Cell

The PEC activity toward the OER was measured for the $\text{Fe}_2\text{O}_3/\text{TiO}_2$ heterostructures. It was shown that the annealing after ALD at 500°C for 30 min can improve the performance of such heterostructures [17, 18, 20]. Therefore, the PEC performance of the samples as-prepared and annealed after ALD was analyzed using a PEC scanning flow cell (SFC). First, a photovoltammogram was collected, and Figure 2a indicates that all $\text{Fe}_2\text{O}_3/\text{TiO}_2$ samples (as-prepared and annealed) present an anodic shift of the photocurrent onset as well as a lower

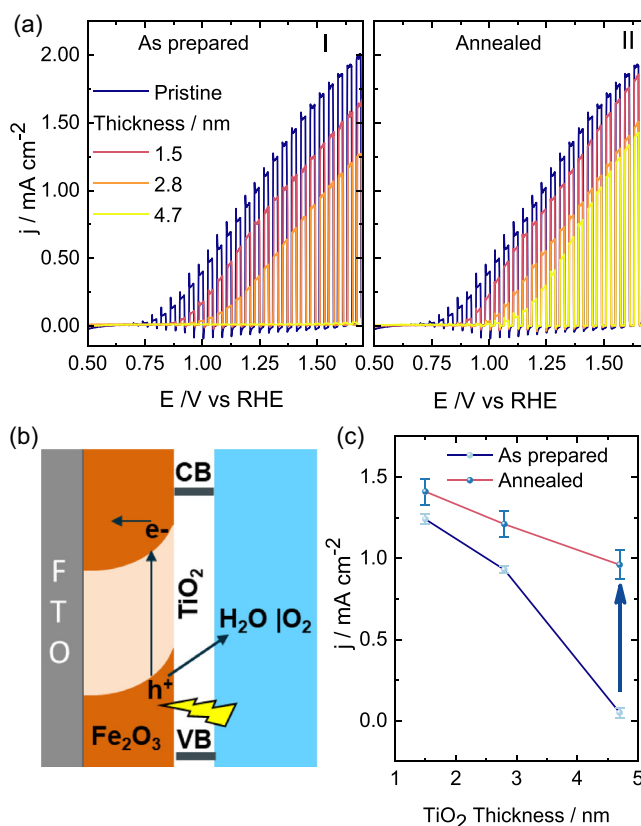


FIGURE 2 | (a) Photovoltammogram of Fe_2O_3 and different $\text{Fe}_2\text{O}_3/\text{TiO}_2$ photoanodes measured in 50 mM NaOH at a scan rate of 10 mV s^{-1} . Panel I displays the as-prepared samples, no further treatment after ALD, while panel II shows the samples annealed after ALD. (b) Scheme of the processes taking place at the $\text{Fe}_2\text{O}_3/\text{TiO}_2$ /electrolyte interface under irradiation, VB stands for valence band and CB stands for conduction band. (c) Photocurrent of the different modified photoanodes during a chronoamperometry at $1.5 V_{\text{RHE}}$. Average values were obtained from 3 measurements on different spots using the same sample, and the error bars represent the standard deviation.

photocurrent value when compared to the bare Fe_2O_3 NR. Both the anodic shift and the decrease in photocurrent scale with the thickness of the TiO_2 overlayer in all samples. For $\text{Fe}_2\text{O}_3/\text{TiO}_2$ heterostructures, the valence band edge alignment is unfavorable for hole transport toward the electrolyte [20] (see scheme in Figure 2b), so the charge transfer across the TiO_2 layer occurs mainly by the tunneling effect [44]. Therefore, the trends observed in the performance of the different as-prepared and annealed $\text{Fe}_2\text{O}_3/\text{TiO}_2$ photoanodes can be understood as the hindering of hole tunneling when the TiO_2 layer gets thicker [20].

Another feature that stands out in the bare samples is the presence of anodic spikes at the beginning of the photocurrent transients (and cathodic spikes once the light is turned off). Notably, the anodic and cathodic spikes decrease upon the deposition of TiO_2 . This effect observed in the photovoltammogram is related to the passivation of trap states that prevent hole accumulation at the interface in the presence of the TiO_2 overlayer [45, 46].

The annealing after the ALD process leads to an increase in activity for all samples (see Figure 1a panel II), although the photocurrent values are still lower than the bare Fe_2O_3 NR. To better

depict the changes in activity for the as-prepared and annealed samples, a chronoamperometry (CA) was recorded at $1.5 V_{\text{RHE}}$ under irradiation, and the mean values of several measurements are plotted in Figure 2c. The trends observed during the photovoltammogram are confirmed, showing a decrease in activity for thicker TiO_2 layers and an enhancement in photocurrent after annealing. The increase in photocurrent after annealing for the sample coated with 4.7 nm TiO_2 is remarkable, improving the photocurrent by 20 times, while the improvement for the 1.5 ± 0.2 and 2.8 ± 0.5 nm coatings is 1.1 and 1.3 times, respectively. Therefore, for the specific case of a 4.7 nm thick TiO_2 coating, the annealing leads to activation of the sample. Similar results were found for Fe_2O_3 nanostructures prepared by spray pyrolysis, reporting a decrease in photocurrent after coating with TiO_2 using ALD [17, 18]. Similarly, the annealing after ALD produced an improvement in the activity. Other studies have related the better performance after annealing due to a higher crystallinity of the TiO_2 coating, which facilitates the transport of the holes toward the electrolyte [47]. Additionally, doping of Fe_2O_3 with Ti(IV), diffusing from the TiO_2 coating, could contribute to improved material performance [36, 37]. Although the annealing conditions employed in this study are not expected to promote a solid-state reaction between TiO_2 and Fe_2O_3 —and, as previously noted, the core-shell structure remains preserved after annealing—the possibility of Ti(IV) doping cannot be entirely ruled out. Even minimal diffusion may significantly influence the PEC response [48]. Furthermore, previous reports have shown that annealing after the deposition of submonolayer TiO_2 by ALD can generate intermediate surface states that enhance the OER [35]. Therefore, the postannealing step may affect the system by inducing Ti(IV) doping, altering the TiO_2 crystal structure, or modifying surface states—all of which can directly impact PEC performance.

The results highlight the importance of postmodification procedures when ALD is used and their impact on the PEC activity of protected photoanodes. Since the annealed $\text{Fe}_2\text{O}_3/\text{TiO}_2$ NR showed better activity, only this group of samples is considered for further stability measurements.

2.3 | Comparison of Performance Losses Using a Long-Term Measurement and an AST

The long-term stability of photoanodes is a crucial property to assess; however, these measurements are time-consuming and can lead to irreproducible results. To overcome this drawback and investigate stability more efficiently, AST was developed as a practical tool that enhances the degradation process in a shorter time scale.

In this study, we aim to investigate the stability of $\text{Fe}_2\text{O}_3/\text{TiO}_2$ heterostructures using the PEC scanning flow cell (PEC-SFC) during an AST. As there is little information in the literature on ASTs applied to photoanodes, we took inspiration from ASTs used for dark OER electrocatalysts [29, 33, 34]. These protocols typically involve alternating short potential pulses or fast CV scans between targeted operational potentials. We consider the AST protocol based on pulses to be suitable for PEC evaluation, as it mimics the effects of startup and shutdown cycles, conditions that PEC devices may encounter due to the intermittent nature of solar irradiation. Specifically, the AST was conducted between OCP and $1.7 V_{\text{RHE}}$ (a potential used for long-term stability measurements) under constant irradiation [17, 49]. Figure 3a illustrates a few experimental cycles recorded in the SFC to showcase the protocol. The resulting photocurrent profile

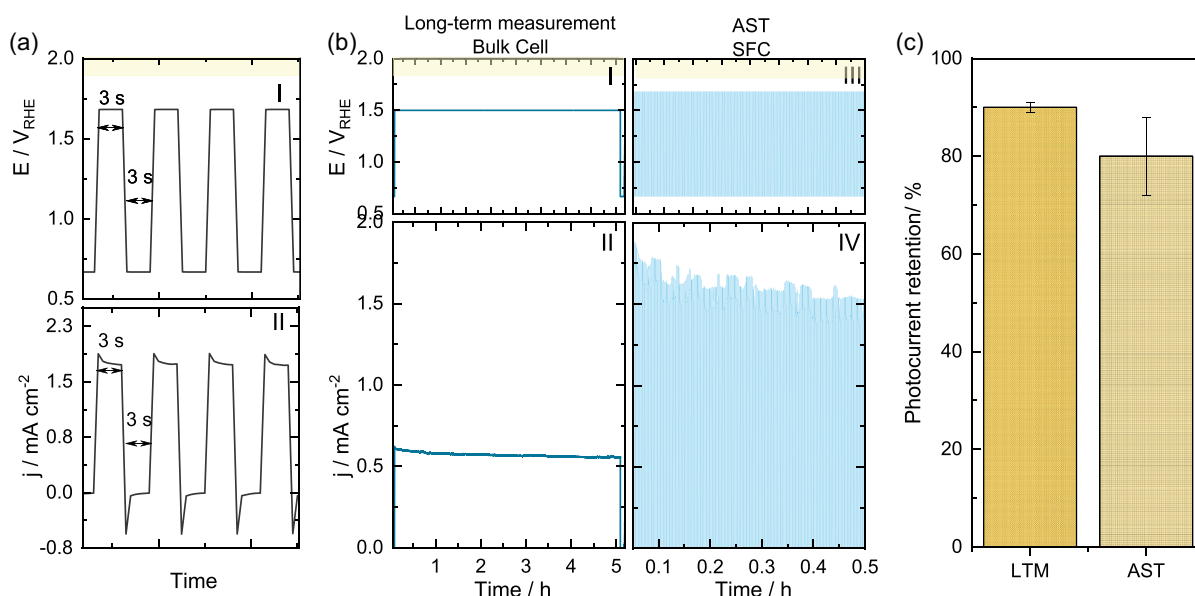


FIGURE 3 | (a) Representative cycles of the AST of bare Fe_2O_3 NR measured in the PEC-SFC using 50 mM NaOH. Panel I displays the potentiostatic profile applied, and panel II shows the corresponding current density. (b) PEC performance of a bare Fe_2O_3 NR photoanode during two types of measurements is shown. First, a long-term measurement was conducted in a three-electrode bulk cell. In this case, panel (I) displays the potentiostatic protocol applied. The bottom panel (II) shows the current density obtained during the long-term measurement. Second, AST was measured using the PEC-SFC. Panel (III) presents the potentiostatic protocol applied. The bottom panel (IV) shows the current density obtained during the AST protocol. The yellow segment allocated above highlights the irradiation period for all previous figures. (c) Comparison of the retention of photocurrent of bare Fe_2O_3 NR after both types of aging. Average values were obtained from 2 repetitions, and the error bars represent the standard deviation.

closely resembles the one observed during the photovoltammogram shown in Figure 2a, showing the expected photocurrent along with the associated anodic and cathodic spikes that have been previously described.

We compared the effects of the selected AST in PEC-SFC on degradation with long-term measurement (LTM) in a conventional three-electrode bulk cell. Figure 3b indicates that the photocurrent measured in the bulk cell is approximately one-third of the photocurrent observed in the PEC-SFC. This lower photocurrent in the bulk-cell is likely due to the larger irradiated area than the PEC-SFC (10 times greater). It has been reported that upscaling photoanode materials generally leads to a lower current density under irradiation [50]. The reduction is attributed to the significant resistance of the fluorine-doped tin oxide (FTO) layer [51]. Also, this effect has been demonstrated in Fe_2O_3 photoanodes, where an increase in length (for a fixed width) resulted in lower photocurrent density despite the larger overall area [52]. Therefore, the lower performance in the bulk cell can be explained in terms of the significantly higher area of the photoanode used in the experimental setup.

The retention of photocurrent is 90% for the LTM, obtaining similar results as other reports in literature, indicating 85% of photocurrent retention in similar time-scale experiments [4, 27], while others show comparable trends in the photocurrent decay during a chronoamperometry [20, 26].

In both the LTM and AST, a decrease in activity is observed over time. The retention of photocurrent is plotted in Figure 3b, showing a similar decline in performance in both cases. Therefore, we concluded that the 300-cycle pulses AST of 30 min generates a performance decrease comparable to a 5-h constant applied potential (CA) measurement in a bulk-cell,

which is an acceptable timescale for PEC-ICP-MS applications. A direct comparison of the photocurrent losses on the same timescale is presented for both protocols in Figure S5, showing that the AST achieves $\sim 10\%$ performance loss in significantly less time.

It is important to note that, although the degradation rate appears similar under both protocols, the underlying mechanisms responsible for the performance losses may differ. Therefore, we emphasize that the two protocols are not equivalent; rather, the AST protocol performed in the SFC can induce performance losses comparable to those observed under constant applied potential in a bulk cell, but on a shorter timescale.

2.4 | Stability of $\text{Fe}_2\text{O}_3/\text{TiO}_2$ Using 1 CV and AST Measured with PEC-ICP-MS

The stability evaluation was performed using two different protocols to compare the AST results with commonly used approaches in PEC-ICP-MS. First, a single CV under dark conditions followed by a single CV under irradiation were recorded with PEC-ICP-MS. Also, the AST described in the previous section was applied to the different $\text{Fe}_2\text{O}_3/\text{TiO}_2$ heterostructures.

Figure 4a shows the stability measurements for the bare and protected Fe_2O_3 NR using the 1 CV cycle. When 1 CV is recorded in the dark, negligible current density is observed, as no significant redox processes take place. This goes in line with the photovoltammograms shown previously, where it was clear for all samples that the interruption of irradiation led to negligible activity up to 1.7 V_{RHE} . No dissolution of Fe is observed in the dark, confirming our previous findings in 50 mM NaOH [15].

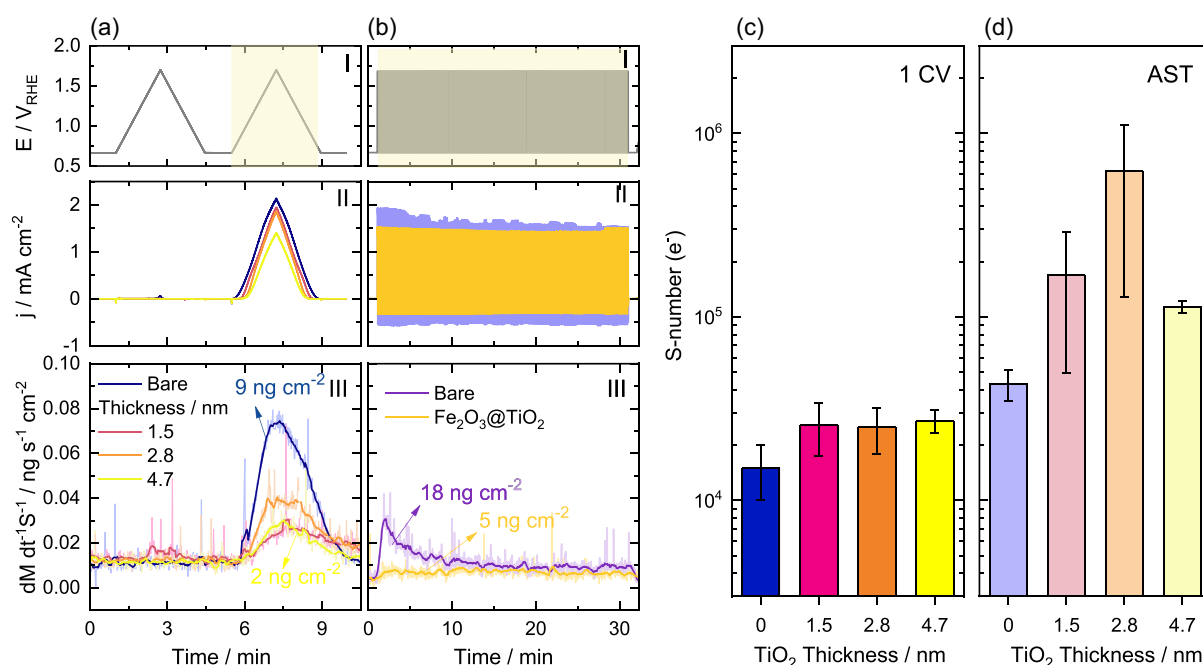


FIGURE 4 | (a) Stability measurement using the PEC-ICP-MS (a) during a series of CVs and (b) during the defined AST. Different panels show I) potentiostatic protocol vs. time also displaying illumination period (yellow area), II) obtained current density, and III) Fe dissolution detected during the measurement. S-number (e^-) calculated from an (c) irradiated CV and (d) the proposed AST.

As the sample is irradiated during the following CV, the photocurrent increases with potential, confirming the trends in activity observed in the previous section. Fe dissolution takes place for the bare Fe₂O₃ NR sample, reaching a peak at 0.07 ng cm⁻² s⁻¹ during the irradiated CV. The Fe dissolution is decreased for all Fe₂O₃@TiO₂ heterostructures, showing peak dissolution in the range of 0.03 ng cm⁻² s⁻¹. Noteworthy, the Fe dissolution decreased to almost the same level for the different TiO₂ thicknesses, suggesting that a TiO₂ coating of 1.5 nm is sufficient to reduce Fe leaching. Similar results were observed for IrO_x@WO₃ photoanodes [24]. Also, Ti dissolution was measured during this protocol (see S6). No Ti leaching was found either during the CV in the dark or under irradiation, or Ti dissolution is under the detection limit of the ICP-MS, confirming that TiO₂ is a material suitable to protect Fe₂O₃ for PEC applications in alkaline electrolyte.

Figure 4b presents stability results for both the bare and the protected sample with 4.7 ± 0.6 nm TiO₂ during the applied AST. The photocurrent measured reveals once again higher activity for the bare sample when compared to the Fe₂O₃@TiO₂ heterostructure, consistent with previous observations.

Throughout the AST, the bare sample exhibits a noticeable decrease in photocurrent, while the protected sample shows only a negligible decline. This observation highlights the superior photocurrent retention during the AST when the Fe₂O₃ NR are coated with 4.7 ± 0.6 nm TiO₂. A dedicated discussion on photocurrent retention after the AST for all samples is developed in Section 2.5.

Regarding Fe dissolution, the bare sample initially shows a peak dissolution rate of 0.03 ng cm⁻² s⁻¹ at the start of the AST, which gradually decreases to a stationary state of approximately 0.01 ng cm⁻² s⁻¹. Notably, the Fe dissolution continues throughout the entire AST, only decreasing once the AST is stopped. During the AST, the Fe₂O₃@TiO₂ heterostructures present a marginal Fe dissolution, reaching a stationary rate of 0.007 ng cm⁻² s⁻¹ more quickly.

Similar trends were found for the Fe₂O₃@TiO₂ samples covered with 1.5 ± 0.2 and 2.8 ± 0.5 nm TiO₂ during the stability evaluation using the AST. As can be observed in Figure S7, lower activity and a decrease in Fe dissolution are observed during the AST.

Similarly, as it was observed during the 1 CV protocol, Ti dissolution during the AST was negligible or under the detection limit of ICP-MS (see S8).

The AST led to a loss of 18 ng cm⁻² of Fe for the unprotected Fe₂O₃, while the protected Fe₂O₃ with a few ALD cycles experienced a loss of 5 ng cm⁻². This result further confirms that TiO₂ protection successfully reduces Fe dissolution during the AST.

The higher peak dissolution rate on the bare Fe₂O₃ NR obtained during a single irradiated CV (0.07 ng cm⁻² s⁻¹) called our attention, when compared to the lower AST peak dissolution rate (0.03 ng cm⁻² s⁻¹). We performed an additional AST consisting of CVs recorded at 200 mV s⁻¹ from OCP to 1.7 V_{RHE}, finding that the CV AST protocol led to higher dissolution rates and total

dissolved Fe than pulses. A dedicated discussion on the results can be found in S9.

To determine the optimal TiO₂ thickness to protect Fe₂O₃ NR, both activity and stability should be evaluated together. The S-number is a metric introduced to compare electrocatalysts by considering both metal dissolution and total O₂ evolved (or electrons exchanged if other than OER reactions are involved). Thus, the S-number is calculated based on the quantification of metal dissolved during a specific protocol, which can be measured using online ICP-MS, and the total amount of O₂ evolved, which is derived from the charge passed under the assumption of 100% Faradaic efficiency for OER.

However, since 100% Faradaic efficiency is not often reported in PEC systems, the S-number (e⁻) for photoanodes was redefined [11], considering the number of electrons (e⁻) passed during a given protocol divided by the number of metallic atoms dissolved (M)

$$S - \text{number}(e^-) = \frac{n(e^-)}{n(M)} \quad (1)$$

The S-number (e⁻) was calculated for the bare and Fe₂O₃@TiO₂ heterostructures using both protocols tested in the PEC-ICP-MS: a single CV under irradiation and the AST. As shown in Figure 4c, the S-number (e⁻), obtained from a single CV, slightly increases when Fe₂O₃ NRs are protected by a TiO₂ layer. In contrast, the S-number (e⁻) quantified from the AST protocol reaches its maximum for the 2.8 nm TiO₂ coating, highlighting a tradeoff between activity and stability when the material is exposed to more severe conditions. Accordingly, an optimal TiO₂ thickness can be identified that enhances stability while maximizing activity during the AST.

The results highlight the use of the AST as a practical approach to probe PEC degradation and monitor metal dissolution in situ. While this protocol is not intended to be a definitive standard, it represents an important first step toward developing reliable long-term stability protocols in the field.

2.5 | PEC Performance Over AST

To investigate the impact of TiO₂ thickness on performance after the AST, we measured the photocurrent at 1.7 V_{RHE} at both the beginning and the end of the AST to calculate the photocurrent decay. Additionally, CVs were measured under irradiation before and after the AST to gather more information about the performance of the photoanodes.

The photocurrent decay is shown in Figure 5a for the bare Fe₂O₃ sample and Fe₂O₃ NRs protected with different TiO₂ thicknesses. A clear trend is observed: as the TiO₂ thickness increases, the photocurrent decay decreases, indicating that a thicker TiO₂ layer helps retain the performance during the AST. This further confirms that TiO₂ deposition via ALD is an effective method to enhance not only the stability but also the photocurrent retention of Fe₂O₃ NRs.

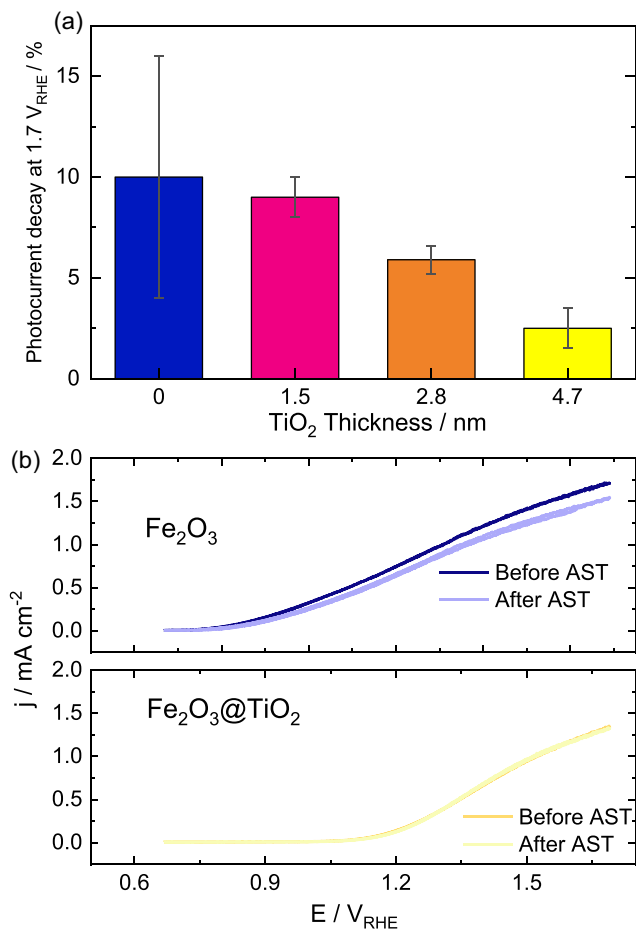


FIGURE 5 | (a) Decay in the photocurrent after the AST for the pristine and protected photoanodes in 50 mM NaOH. Average values were obtained from 3 measurements in different spots, and the error bars represent the standard deviation. (b) CVs at a scan rate of 10 mV s⁻¹ measured previous and after the AST for bare and Fe₂O₃@TiO₂ covered photoanodes with 4.7 nm of TiO₂.

The CV results before and after the AST also support this trend (see Figure 5b). For the bare Fe₂O₃ sample, a decrease in photocurrent is observed across all potentials after the AST, while the change is minimal for the sample with a TiO₂ coating of 4.7 nm. The CVs measured for the 1.5 ± 0.2 and 2.8 ± 0.5 nm TiO₂ coatings are provided in S10.

The cause of the photocurrent decrease in Fe₂O₃ is not fully understood yet. It has been suggested that Fe dissolved in alkaline media comes from material detachment during operation due to mechanical erosion by the OER [53]. However, ALD might not significantly improve adhesion to FTO. Also, the consumption of OH⁻ during OER could decrease pH locally if the photocurrent is high enough, leading to dissolution of Fe due to increased acidity in the vicinity of the photoanode [13]. On the other hand, it was reported that after prolonged operation in alkaline electrolyte (up to 70 h) FeOOH structures are detected [54]. Further, it was demonstrated that the use of neutral electrolytes containing phosphate buffers can directly react with Fe₂O₃ [15, 55], leading to surface modification and possibly degradation. These results indicate that subtle surface reconstruction takes place in Fe₂O₃ photoanodes during long-term operation

in different electrolytes and might be the reason for the decrease in performance observed. Therefore, we hypothesize that processes such as Fe dissolution and redeposition of inactive Fe species, leading finally to surface reconstruction, can occur at the surface and interfere with the critical process of hole transfer to the electrolyte during OER. Given the decrease in Fe dissolution and improvement in photocurrent retention with TiO₂ overlayers, it is possible that surface reconstruction is mitigated, and the performance is better retained over time.

Thus, optimizing the TiO₂ coating thickness is crucial to preventing dissolution under PEC conditions and minimizing performance loss during AST.

3 | Conclusions and Outlook

In this work, we investigated the stability and PEC performance of Fe₂O₃ NRs protected with TiO₂ of different thicknesses obtained by ALD. To assess stability, we combined AST with online PEC-ICP-MS characterization. The AST protocol successfully replicated long-term degradation trends within a shorter timeframe, proving to be an effective tool for rapid stability assessment. Our results demonstrate that the TiO₂ overlayer significantly improves the stability of Fe₂O₃ by reducing photocorrosion, while its thickness plays a critical role in balancing activity and protection. Also, our results highlight that it is necessary to include a post-ALD annealing to improve the performance of thinner TiO₂ or even activate the samples with thicker TiO₂ coatings. Increasing the TiO₂ thickness reduces Fe dissolution but also leads to lower PEC activity. We consider that a conformal coating of 2.8 nm TiO₂ prepared by ALD leads to an optimal condition, minimizing degradation while maintaining acceptable photocurrent performance. These insights highlight the importance of ASTs and PEC-ICP-MS to engineer protective layers and improve the stability of photoanodes in PEC applications.

4 | Experimental

4.1 | Synthesis of Fe₂O₃ Nanorods

Fe₂O₃ nanorods were synthesized on an FTO glass substrate (TEC15, Sigma-Aldrich) using an adapted hydrothermal method optimized previously [15].

4.2 | Preparation of the Fe₂O₃@TiO₂ Photoanodes

The TiO₂ overlayers were grown on hematite using a commercial LD reactor Gemstar-6 XT by Arradiance. The Fe₂O₃ surfaces were cleaned preliminarily using ozone during 30 min. For ALD, titanium (IV) isopropoxide (TTIP) was used as a metal precursor while ultrapure water was used as the oxygen source. The canister containing the iron precursor ferrocene was heated to 70°C, and water was kept at room temperature, while the manifold and reaction chamber were maintained at 100°C, and 150°C, respectively. The precursors were introduced into the ALD chamber in a sequence using N₂ as purging and carrier gas. For the

TTIP precursor the pulse time, exposure time and purge time were 0.8, 50, and 70 s. For water, the pulse time, exposure time, and purge time were 0.5, 50 s. This whole sequence consisted of 1 ALD cycle. The Fe_2O_3 photoanodes were covered using 25, 50, and 75 cycles. After ALD, the $\text{Fe}_2\text{O}_3/\text{TiO}_2$ samples were annealed at 500°C for 30 min.

4.3 | Morphological Characterization

The structure of the synthesized Fe_2O_3 and $\text{Fe}_2\text{O}_3/\text{TiO}_2$ samples was investigated using high-resolution scanning transmission electron microscopy (HR-STEM). Measurements were performed using a Talos F200i from Thermo Fisher Scientific operated at an acceleration voltage of 200 kV. The microscope features an X-FEG and a Dual Bruker XFlash 6T-100 EDS detector. The beam current was set to 240 pA, and a high-angle annular dark field (HAADF) detector was used for imaging. The crystal structure of the $\text{Fe}_2\text{O}_3/\text{TiO}_2$ samples was analyzed by X-ray diffraction in Bragg-Brentano (BB-XRD) using a Bruker D8 Advance equipped with a Cu K α source and LynxEye XE detector.

4.4 | PEC-ICP-MS Measurements

The PEC performance of the Fe_2O_3 and $\text{Fe}_2\text{O}_3/\text{TiO}_2$ samples was characterized using a previously reported SFC setup [9]. The SFC was constructed from polytetrafluoroethylene and connected to the counter electrode (a glassy carbon rod), the reference electrode (Metrohm Ag/AgCl, 3 M KCl), and an inductively coupled plasma mass spectrometer (ICP-MS; PerkinElmer NexION 300) via Tygon tubing. The electrolyte reservoir was constantly purged with Ar (5.0, AirLiquide). The working electrode was placed on a movable stage (Physical Instruments) to establish contact with the SFC opening (0.059 cm² area). Copper tape was used to ensure electrical contact with the working electrode. Electrochemical measurements were performed using a Gamry REF600 potentiostat. The recorded potentials were converted to the reversible hydrogen electrode (RHE) scale using the following equation

$$E_{\text{RHE}} = E_{\text{Ag|AgCl}} + 0.197\text{V} + 0.059\text{pH}$$

The optical setup for the PEC-ICP-MS system was previously described in detail [9]. To simulate the solar spectrum and intensity on the electrode, light from a 300 W ozone-free xenon lamp (Newport) was passed through an AM 1.5G filter (Newport) and directed into the PEC-SFC via a liquid light guide (Newport). The light intensity at the SFC opening was adjusted to 100 mW cm⁻² every day before measurements, using a calibrated photovoltaic cell normalized to the 0.059 cm² illumination area. Electrolytes were prepared with NaOH.H₂O (99.99% suprapur, Merck) containing low Fe impurities, and DI water (Merck, Milli-Q). The ICP-MS was calibrated in a daily basis for Fe and Ti with freshly prepared standards (Merck Certipur) using a four-point calibration with the following solutions: 0, 0.5, 1.0, and 5.0 $\mu\text{g L}^{-1}$. A solution containing a concentration of Co and Sc standard of 10 $\mu\text{g L}^{-1}$ served as the internal standard for Fe and Ti, respectively. To handle the interference of $^{56}\text{Fe}^+$ with the specie $^{40}\text{Ar}^{16}\text{O}^+$, a dynamic reaction cell (DRC) with methane was used

in all measurements involving the quantification of Fe. On the other hand, Ti was quantified in standard mode during the 1 CV protocol, and using the DRC mode during the AST to simplify the measurements.

4.5 | Bulk-Cell Measurements

The measurement to establish the performance decay after operation over 5 h was conducted using a commercial PEC three-electrode cell (PEC 15 . 15 mm², redox.me), which included an Ag|AgCl reference electrode and a graphite rod as the counter electrode. The light source was provided by the same optical setup used in the PEC-ICP-MS, employing a liquid light guide to irradiate the working electrode from the back (0.5 cm²). The electrolyte, 50 mM NaOH, was purged with Ar (5.0, AirLiquide) for 15 min before each measurement, and an Ar flow was maintained through the gas inlet/outlet of the bulk cell during the experiment.

Acknowledgments

V.B.L. acknowledges the Alexander von Humboldt Foundation for granting a Postdoctoral Fellowship (Georg Forster program), Jonas Möller for software development for data analysis used in this work, and Christian Göllner and Matej Zlatar for all the required technical support during ICP-MS measurements.

Open Access funding enabled and organized by Projekt DEAL.

Conflicts of Interest

The authors declare no conflicts of interest.

Data Availability Statement

The data that support the findings of this study are available from the corresponding author upon reasonable request.

References

1. B. Liu, Z. Qian, X. Shi, et al., "Solar-Driven Selective Conversion of Millimolar Dissolved Carbon to Fuels with Molecular Flux Generation," *Nature Communications* 16, no. 1 (2025): 1558, <https://doi.org/10.1038/s41467-025-56106-3>.
2. P. P. Kunturu, S. Bera, H. Johnson, and M. N. Tsampas, "Scaled-Up Zero-Gap Photoelectrochemical Device Based on Abundant Materials for Bias-Free Solar Hydrogen Production," *Artificial Photosynthesis* 1 (2025):106–116, <https://doi.org/10.1021/aps.4c0002310.1021/aps.4c00023>.
3. J. Park, K.-Y. Yoon, B. G. Ghule, H. Kim, and J.-H. Jang, "Morphology-Engineered Hematite Photoanode for Photoelectrochemical Water Splitting," *ACS Energy Letters* 9, no. 6 (2024): 3169–3176, <https://doi.org/10.1021/acsenergylett.4c01347>.
4. H. Kong, J. S. Park, J. H. Kim, S. Hwang, and J. Yeo, "Hydrothermal Synthesis in Gap: Conformal Deposition of Textured Hematite Thin Films for Efficient Photoelectrochemical Water Splitting," *Acs Applied Materials & Interfaces* 14, no. 14 (2022): 16515, <https://doi.org/10.1021/acsami.2c00128>.
5. C. Xu, H. Wang, H. Guo, et al., "Parallel Multi-Stacked Photoanodes of Sb-Doped p-n Homojunction Hematite with Near-Theoretical Solar Conversion Efficiency," *Nature Communications* 15, no. 1 (2024): 9712, <https://doi.org/10.1038/s41467-024-53967-y>.

6. Y. Zhang, B. Liu, L. Xu, Z. Ding, R. Yang, and S. Wang, "Failure Mechanism Analysis and Emerging Strategies for Enhancing the Photoelectrochemical Stability of Photoanodes," *ChemSusChem* 18 (2025): e202401420, <https://doi.org/10.1002/cssc.202401420>.
7. F. Nandjou and S. Haussener, "Degradation in Photoelectrochemical Devices: Review with an Illustrative Case Study," *Journal of Physics D: Applied Physics* 50, no. 12 (2017): 124002, <https://doi.org/10.1088/1361-6463/aa5b11>.
8. F. Nandjou and S. Haussener, "Kinetic Competition between Water-Splitting and Photocorrosion Reactions in Photoelectrochemical Devices," *ChemSusChem* 12, no. 9 (2019): 1984, <https://doi.org/10.1002/cssc.201802558>.
9. K. J. Jenewein, A. Kormányos, J. Knöppel, K. J. J. Mayrhofer, and S. Cherevko, "Accessing In Situ Photocorrosion under Realistic Light Conditions: Photoelectrochemical Scanning Flow Cell Coupled to Online ICP-MS," *ACS Measurement Science* 1, no. 2 (2021): 74–81, <https://doi.org/10.1021/acsmeasuresciau.1c00016>.
10. S. Zhang, M. Rohloff, O. Kasian, et al., "Dissolution of BiVO₄ Photoanodes Revealed by Time-Resolved Measurements under Photoelectrochemical Conditions," *The Journal of Physical Chemistry C* 123 (2019): 38, <https://doi.org/10.1021/acs.jpcc.9b07220>.
11. J. Knöppel, A. Kormányos, B. Mayerhöfer, et al., "Photocorrosion of WO₃ Photoanodes in Different Electrolytes," *ACS Physical Chemistry Au* 1, no. 1 (2021): 6–13, <https://doi.org/10.1021/acsphyschemau.1c00004>.
12. J. Knöppel, S. Zhang, F. D. Speck, K. J. J. Mayrhofer, C. Scheu, and S. Cherevko, "Time-Resolved Analysis of Dissolution Phenomena in Photoelectrochemistry – A Case Study of WO₃ Photocorrosion," *Electrochemistry Communications*, 96 (2018): 53–56, <https://doi.org/10.1016/j.elecom.2018.09.008>.
13. K. J. Jenewein, Y. Wang, T. Liu, et al., "Electrolyte Engineering Stabilizes Photoanodes Decorated with Molecular Catalysts," *ChemSusChem* 16 (2023): e202202319, <https://doi.org/10.1002/cssc.202202319>.
14. K. J. Jenewein, S. Thienhaus, A. Kormányos, A. Ludwig, and S. Cherevko, "High-Throughput Exploration of Activity and Stability for Identifying Photoelectrochemical Water Splitting Materials," *Chemical Science* 13, no. 46 (2022): 13774, <https://doi.org/10.1039/d2sc05115j>.
15. V. Benavente Llorente, K. J. Jenewein, M. Bierling, et al., "Photocorrosion of Hematite Photoanodes in Neutral and Alkaline Electrolytes," *The Journal of Physical Chemistry C* 127 (2023): 39, <https://doi.org/10.1021/acs.jpcc.3c02969>.
16. S. Zhang, I. Ahmet, S. H. Kim, et al., "Different Photostability of BiVO₄ in Near-pH-Neutral Electrolytes," *Acs Applied Energy Materials* 3, no. 10 (2020): 9523–9527, <https://doi.org/10.1021/acsaem.0c01904>.
17. T. Imrich, H. Krýsová, M. Neumann-Spallart, and J. Krýsa, "Fe₂O₃ Photoanodes: Photocorrosion Protection by Thin SnO₂ and TiO₂ Films," *Journal of Electroanalytical Chemistry* 892 (2021): 115282, <https://doi.org/10.1016/j.jelechem.2021.115282>.
18. T. Imrich, R. Zazpe, H. Krýsová, et al., "Protection of Hematite Photoelectrodes by ALD-TiO₂ Capping," *Journal of Photochemistry and Photobiology A: Chemistry* 409 (2021): 113126, <https://doi.org/10.1016/j.jphotochem.2020.113126>.
19. T. Imrich, M. Neumann-Spallart, H. Krýsová, H. Tarábková, R. Nebel, and J. Krýsa, "Ti Doped Hematite Photoanodes: Protective Coverage by Titania Overlayers," *Journal of Photochemistry and Photobiology A: Chemistry* 445 (2023): 115026, <https://doi.org/10.1016/j.jphotochem.2023.115026>.
20. J. Wang, L. Liccardo, H. Habibimarkani, et al., "Precise Control of TiO₂ Overlayer on Hematite Nanorod Arrays by ALD for the Photoelectrochemical Water Splitting," *Sustainable Energy & Fuels* 8, no. 16 (2024): 3753–3763, <https://doi.org/10.1039/d3se01633a>.
21. D. Barreca, G. Carraro, M. E. A. Warwick, et al., "Fe₂O₃–TiO₂nanosystems by a Hybrid PE-CVD/ALD Approach: Controllable Synthesis, Growth Mechanism, and Photocatalytic Properties," *CrystEngComm* 17, no. 32 (2015): 6219–6226, <https://doi.org/10.1039/c5ce00883b>.
22. J. Krýsa, A. Němečková, M. Zlámál, et al., "α-Fe₂O₃/TiO₂ Stratified Photoanodes," *Journal of Photochemistry and Photobiology A: Chemistry* 366 (2018): 12–17, <https://doi.org/10.1016/j.jphotochem.2018.03.015>.
23. P. Dias, T. Lopes, L. Andrade, and A. Mendes, "Temperature Effect on Water Splitting Using a Si-Doped Hematite Photoanode," *Journal of Power Sources* 272 (2014): 567–580, <https://doi.org/10.1016/j.jpowsour.2014.08.108>.
24. K. J. Jenewein, J. Knöppel, A. Hofer, et al., "Dissolution of WO₃ Modified with IrO_x Overlayers during Photoelectrochemical Water Splitting," *SusMat* 3, no. 1 (2023): 128–136, <https://doi.org/10.1002/sus2.107>.
25. N. Pastukhova, A. Mavrič, and Y. Li, "Atomic Layer Deposition for the Photoelectrochemical Applications," *Advanced Materials Interfaces* 8, no. 7 (2021): 2002100, <https://doi.org/10.1002/admi.202002100>.
26. G. Liu, Y. Zhao, R. Yao, et al., "Realizing High Performance Solar Water Oxidation for Ti-Doped Hematite Nanoarrays by Synergistic Decoration with Ultrathin Cobalt-Iron Phosphate Nanolayers," *Chemical Engineering Journal* 355 (2019): 49–57, <https://doi.org/10.1016/j.cej.2018.08.100>.
27. F. Feng, C. Li, J. Jian, X. Qiao, H. Wang, and L. Jia, "Boosting Hematite Photoelectrochemical Water Splitting by Decoration of TiO₂ at the Grain Boundaries," *Chemical Engineering Journal* 368 (2019): 959–967, <https://doi.org/10.1016/j.cej.2019.03.005>.
28. D. Delgado, F. Bizzotto, A. Zana, and M. Arenz, "Accelerated Durability Test for High-Surface-Area Oxyhydroxide Nickel Supported on Raney Nickel as Catalyst for the Alkaline Oxygen Evolution Reaction," *Chemphyschem* 20, no. 22 (2019): 3147, <https://doi.org/10.1002/cphc.201900195>.
29. C. Lafforgue, M. Chatenet, L. Dubau, and D. R. Dekel, "Accelerated Stress Test of Pt/C Nanoparticles in an Interface with an Anion-Exchange Membrane—An Identical-Location Transmission Electron Microscopy Study," *ACS Catalysis* 8, no. 2 (2018): 1278–1286, <https://doi.org/10.1021/acscatal.7b04055>.
30. R. Petrone, D. Hissel, M. C. Péra, D. Chamagne, and R. Gouriveau, "Accelerated Stress Test Procedures for PEM Fuel Cells under Actual Load Constraints: State-of-Art and Proposals," *International Journal of Hydrogen Energy* 40, no. 36 (2015): 12489, <https://doi.org/10.1016/j.ijhydene.2015.07.026>.
31. N. Li, S. S. Araya, and S. K. Kær, "Investigating Low and High Load Cycling Tests as Accelerated Stress Tests for Proton Exchange Membrane Water Electrolysis," *Electrochimica Acta* 370 (2021): 137748, <https://doi.org/10.1016/j.electacta.2021.137748>.
32. E. R. Cofell, Z. Park, U. O. Nwabara, et al., "Potential Cycling of Silver Cathodes in an Alkaline CO₂Flow Electrolyzer for Accelerated Stress Testing and Carbonate Inhibition," *ACS Applied Energy Materials* 5, no. 10 (2022): 12013–12013, <https://doi.org/10.1021/acsaem.2c01308>.
33. E. Pizzutillo, S. Geiger, J. P. Grote, et al., "On the Need of Improved Accelerated Degradation Protocols (ADPs): Examination of Platinum Dissolution and Carbon Corrosion in Half-Cell Tests," *Journal of the Electrochemical Society* 163, no. 14 (2016): F1510, <https://doi.org/10.1149/2.0731614jes>.
34. T. Priamushko, E. Franz, A. Logar, et al., "Be Aware of Transient Dissolution Processes in Co(3)O(4) Acidic Oxygen Evolution Reaction Electrocatalysts," *Journal of the American Chemical Society* 147, no. 4 (2025): 3517, <https://doi.org/10.1021/jacs.4c14952>.
35. L. Palmolahti, H. Ali-Löytty, R. Khan, J. Saari, N. V. Tkachenko, and M. Valden, "Modification of Surface States of Hematite-Based Photoanodes by Submonolayer of TiO₂ for Enhanced Solar Water

- Splitting," *The Journal of Physical Chemistry C* 124, no. 24 (2020): 13094, <https://doi.org/10.1021/acs.jpcc.0c00798>.
36. D. Wang, H. Chen, G. Chang, et al., "Uniform Doping of Titanium in Hematite Nanorods for Efficient Photoelectrochemical Water Splitting," *Acs Applied Materials & Interfaces* 7, no. 25 (2015): 14072, <https://doi.org/10.1021/acsami.5b03298>.
37. X. Li, P. S. Bassi, P. P. Boix, Y. Fang, and L. H. Wong, "Revealing the Role of TiO₂ Surface Treatment of Hematite Nanorods Photoanodes for Solar Water Splitting," *Acs Applied Materials & Interfaces* 7, no. 31 (2015): 16960–16966, <https://doi.org/10.1021/acsami.5b01394>.
38. A. Körner, B. Fritsch, A. L. Morales, P. Malgaretti, and A. Hutzler, "Panta Rhei - Tuning Silver Nanostructure Evolution with Flow and Radiolysis in Liquid Phase STEM," *Nano Today* 61 (2025): 102575, <https://doi.org/10.1016/j.nantod.2024.102575>.
39. P. Qiu, H. Yang, L. Yang, Q. Wang, and L. Ge, "Solar Water Splitting with Nanostructured Hematite: The Role of Annealing-Temperature," *Electrochimica Acta* 266 (2018): 431–440, <https://doi.org/10.1016/j.electacta.2018.02.030>.
40. Y. Ling, G. Wang, D. A. Wheeler, J. Z. Zhang, and Y. Li, "Sn-Doped Hematite Nanostructures for Photoelectrochemical Water Splitting," *Nano Letters* 11, no. 5 (2011): 2119–2125, <https://doi.org/10.1021/nl200708y>.
41. B. Fritsch, M. Wu, A. Hutzler, et al., "Sub-Kelvin Thermometry for Evaluating the Local Temperature Stability Within in Situ TEM Gas Cells," *Ultramicroscopy* 235 (2022): 113494, <https://doi.org/10.1016/j.ultramic.2022.113494>.
42. H. Kohl and L. Reimer, *Transmission Electron Microscopy. Physics of Image Formation* (Springer New York, 2008).
43. T. A. Al-Dhahir and I. Al-Haitham, "Quantitative Phase Analysis for Titanium Dioxide from X-Ray Powder Diffraction Data Using the Rietveld Method," *Diyala Journal for Pure Sciences*, 9 (2013): 108–119.
44. R. Liu, Z. Zheng, J. Spurgeon, and X. Yang, "Enhanced Photoelectrochemical Water-Splitting Performance of Semiconductors by Surface Passivation Layers," *Energy & Environmental Science* 7, no. 8 (2014): 2504–2517, <https://doi.org/10.1039/c4ee00450g>.
45. M. G. Ahmed, I. E. Kretschmer, T. A. Kandiel, A. Y. Ahmed, F. A. Rashwan, and D. W. Bahnemann, "A Facile Surface Passivation of Hematite Photoanodes with TiO₂ Overlayers for Efficient Solar Water Splitting," *Acs Applied Materials & Interfaces* 7, no. 43 (2015): 24053, <https://doi.org/10.1021/acsami.5b07065>.
46. L. M. Peter, "Energetics and Kinetics of Light-Driven Oxygen Evolution at Semiconductor Electrodes: The Example of Hematite," *Journal of Solid State Electrochemistry* 17, no. 2 (2013): 315–326, <https://doi.org/10.1007/s10008-012-1957-3>.
47. Y. Kusumawati, M. Hosni, M. A. Martoprawiro, S. Cassaignon, and T. Pauporté, "Charge Transport and Recombination in TiO₂ Brookite-Based Photoelectrodes," *The Journal of Physical Chemistry C* 118, no. 41 (2014): 23459, <https://doi.org/10.1021/jp5047479>.
48. S. Zhang, S. Zhang, W. Leng, and D. Wu, "Ti Doped α -Fe₂O₃ Electrodes for Water Oxidation," *Journal of Alloys and Compounds* 927 (2022): 166975, <https://doi.org/10.1016/j.jallcom.2022.166975>.
49. T. T. Hien, N. D. Quang, N. M. Hung, et al., "Sn Doping into Hematite Nanorods for High-Performance Photoelectrochemical Water Splitting," *Journal of the Electrochemical Society* 166, no. 15 (2019): H743, <https://doi.org/10.1149/2.0621914jes>.
50. W. J. Lee, P. S. Shinde, G. H. Go, and E. Ramasamy, "Ag Grid Induced Photocurrent Enhancement in WO₃ Photoanodes and Their Scale-up Performance toward Photoelectrochemical H₂ Generation," *International Journal of Hydrogen Energy* 36, no. 9 (2011): 5262, <https://doi.org/10.1016/j.ijhydene.2011.02.013>.
51. I. Y. Ahmet, Y. Ma, J.-W. Jang, et al., "Demonstration of a 50 cm² BiVO₄ Tandem Photoelectrochemical-Photovoltaic Water Splitting Device," *Sustainable Energy & Fuels* 3, no. 9 (2019): 2366–2379, <https://doi.org/10.1039/c9se00246d>.
52. A. Vilanova, T. Lopes, C. Spence, M. Wullenkord, and A. Mendes, "Optimized Photoelectrochemical Tandem Cell for Solar Water Splitting," *Energy Storage Materials* 13 (2018): 175–188, <https://doi.org/10.1016/j.ensm.2017.12.017>.
53. P. Dias, A. Vilanova, T. Lopes, L. Andrade, and A. Mendes, "Extremely Stable Bare Hematite Photoanode for Solar Water Splitting," *Nano Energy* 23 (2016): 70–79, <https://doi.org/10.1016/j.nanoen.2016.03.008>.
54. J. Xie, P. Yang, X. Liang, and J. Xiong, "Self-Improvement of Ti: Fe₂O₃ Photoanodes: Photoelectrocatalysis Improvement after Long-Term Stability Testing in Alkaline Electrolyte," *ACS Applied Energy Materials* 1, no. 6 (2018): 2769–2775, <https://doi.org/10.1021/acsaem.8b00445>.
55. S. Haschke, D. Pankin, Y. Petrov, S. Bochmann, A. Manshina, and J. Bachmann, "Design Rules for Oxygen Evolution Catalysis at Porous Iron Oxide Electrodes: A 1000-Fold Current Density Increase," *ChemSusChem* 10, no. 18 (2017): 3644–3651, <https://doi.org/10.1002/cssc.201701068>.

Supporting Information

Additional supporting information can be found online in the Supporting Information section. **Supporting Fig. S1:** STEM-EDX spectrum images of Fe₂O₃ nanorods (Fe and Ti signal) coated with 75 ALD cycles (a) as prepared after ALD, (c) annealed at 500°C for 30 min after ALD and corresponding line profiles (50 px average) of Ti and Fe of individual particles. **Supporting Fig. S2:** The thickness of the TiO₂ overlayer for the different ALD cycles used determined through HAADF-STEM on Fe₂O₃ NR, and through ellipsometry on silicon monitor wafers. **Supporting Fig. S3:** XRD of the sample with 75 ALD cycles annealed. **Supporting Fig. S4:** Zoom-in (a) and overview (b) HAADF-STEM and corresponding STEM-EDX spectrum images of the photoelectrode structure in which a dense layer of hematite particles (ca. 200 nm) on top of an SnO₂ layer (ca. 400 nm), both coated onto an SiO₂ substrate, is visible. In XRD measurements, the diffraction signal of the SnO₂ layer overshines most of the hematite signal as well as the entire TiO₂ signal. **Supporting Fig. S5:** (a) Comparison of photocurrent profiles recorded during the AST and the long-term measurement on the same timescale. (b) Enlarged view of the photocurrent decay during the AST, overlaid with the photocurrent evolution in the bulk cell over the first 30 min. **Supporting Fig. S6:** Stability measurement of Fe₂O₃@TiO₂ heterostructures using the PEC-ICP-MS during a series of CVs. Different panels show I) Potentiostatic protocol vs. time also displaying illumination period (yellow area) II) Obtained current density II) Ti dissolution detected during the measurement using standard mode. **Supporting Fig. S7:** Stability measurement using the PEC-ICP-MS during the AST for samples with (a) 2.2 nm and (b) 2.8 nm. Different panels show I) Potentiostatic protocol vs. time also displaying illumination period (yellow area) II) Obtained current density II) Fe dissolution detected during the measurement. **Supporting Fig. S8:** Stability measurement using the PEC-ICP-MS during the AST for all Fe₂O₃@TiO₂. Different panels show I) potentiostatic protocol consisting of alternating pulses (3 s at OCP and 3 s at 1.7 VRHE) vs. time also displaying illumination period (yellow area) II) Obtained current density during the AST II) Ti dissolution detected during the AST. **Supporting Fig. S9:** Stability measurement using the PEC-ICP-MS during the AST for bare samples. Different panels show I) Potentiostatic protocol vs. time also displaying illumination period (yellow area) II) Obtained current density II) Fe dissolution detected during the measurement. **Supporting Fig. S10:** CVs at a scan rate of 10 mV s⁻¹ measured before and after the AST for Fe₂O₃@TiO₂ covered photoanodes with a) 25 cycles of ALD (1.5 ± 0.2 nm TiO₂) and b) 50 cycles of ALD (2.8 ± 0.5 nm TiO₂).